# Pressure Control of Large Cryogenic Tanks in Microgravity

Charles Panzarella [a,*], David Plachta [b], Mohammad Kassemi [c]

[a] *Ohio Aerospace Institute, 22800 Cedar Point Rd., Cleveland, OH 44142, USA*

[b] *NASA Glenn Research Center, 21000 Brookpark Rd., Cleveland, OH 44135, USA*

[c] *National Center for Microgravity Research, NASA Glenn Research Center, 21000 Brookpark Rd., Cleveland, OH 44135, USA*

---

## Abstract

This work studies the pressure control of a large cryogen storage tank in microgravity using a series of parametric numerical simulations. The complete governing equations in the liquid region are coupled to a lumped thermodynamic treatment of the vapor region. It is shown that even in microgravity buoyancy effects rapidly bring the vapor region up to the tank wall. Long-term pressurization studies show that natural convection still leads to considerable thermal stratification in the liquid. A subcooled liquid jet is used to control the pressure rise. At its lowest speed, the jet cannot penetrate far enough into the liquid region to cool the vapor because of retarding buoyancy forces. As the jet speed is increased, it is shown to be quite effective at disrupting the thermal stratification and reducing the tank pressure in a reasonable amount of time.

*Key words:* Zero Boil Off, CFD, Two-Phase Flow (C), Vapor Pressure (C), Space Cryogenics (F)

---

## 1 Introduction

The extension of human space exploration from low Earth orbit into the further reaches of the solar system is one of NASA's biggest challenges for the next millennium. The projected exploration programs include a series of human and robotics expeditions to low and high Earth orbit, the Moon, Mars and possibly to the asteroids and other planetary moons.

---

[*] Corresponding Author. Tel.: (440) 413-1097; fax: (216) 433-5033
*Email address:* `Charles.H.Panzarella@grc.nasa.gov` (Charles Panzarella).

With the exception of extremely short-duration missions, significant cost savings can be achieved if the launch mass can be reduced by improving the cryogenic storage and transfer technologies [1]. Cryogen vaporization is one of the main causes of mass loss and leads to the self-pressurization of the storage tanks. Vaporization can occur during the filling process or may be caused by heat leaks into the tank from the surrounding environment. Ordinarily, the excess pressure can be relieved by direct venting to the environment. For on-surface applications, such as those on the surface of the Earth, Moon or Mars, the spatial configuration of liquid and vapor is dictated by gravity and is well known. In this situation, continuous venting can be easily accomplished, but over a significant length of time it results in considerable cryogen mass loss. For in-space applications, the spatial configuration of liquid and vapor is generally unknown, and direct venting without pre-positioning of the two phases is precluded due to the possibility of expelling liquid along with the vapor. Moreover, venting in space is also undesirable because it prohibits manned flight operations around the storage tanks.

Therefore, from both safety and cryogen conservation viewpoints, a ventless pressure control strategy is highly desirable for both on-surface and in-space applications. The zero boil-off (ZBO) pressure control strategy has been proposed as an effective means of achieving ventless storage through the synergetic application of active cooling and forced mixing [2]. This can be accomplished by using cryocoolers along with impellers, liquid jets or spray bars. The transport mechanisms in such a situation can be extremely complex and require hand-in-hand experimental and theoretical elucidation before being applied in practice.

The self-pressurization of cryogen storage tanks has been the subject of many previous experimental investigations (see Panzarella and Kassemi [3] for a somewhat comprehensive list), but very few have considered the differences due to reduced-gravity conditions. One such work [4] shows that the initial rate of pressurization is lower under reduced-gravity conditions than under normal-gravity conditions, and this was primarily attributed to an increase in the tank wall surface area covered by liquid. Other aspects of cryogen storage have been considered such as the effect of a liquid jet on the bulk mixing behavior [5,6] and its ability to control the tank pressure [7] and reduce thermal stratification [8].

Previous numerical studies of tank pressurization have been primarily limited to purely thermodynamic treatments [9–11], fluid flow and thermal stratification in the liquid without any consideration of the resultant pressure rise in the vapor [12–17], or the evolution of the phase distribution without any thermal considerations [18–25].

Panzarella and Kassemi [3] have developed a more comprehensive numerical model by coupling a lumped thermodynamic treatment of the vapor region with a direct numerical simulation of the Navier–Stokes, energy and continuity equations in the liquid region. In this way, the effect of the heat and mass transport in the liquid region on the tank pressure rise can be determined. This approach has already been used to investigate the pressurization of a small ground-based tank [3] as well as a larger tank in both zero gravity and microgravity environments [26]. It was shown that the initial rate of pressurization depends on the particular heat flux distribution prescribed on the tank wall even though the final rate of pressurization agrees with a purely thermodynamic description of the entire tank. It was also shown that the pressure rise in a ground-based tank could be controlled by using a subcooled liquid jet.

The present work investigates the plausibility of controlling the pressure rise for a large tank in microgravity by using a subcooled liquid jet. In microgravity the vapor region could be anywhere in the tank, but it will be shown that it still tends to migrate towards the tank wall rather quickly due to residual buoyancy forces. Consequently, long-term pressurization is examined with the vapor region fixed near the tank wall. It is shown that pressure control can be achieved in this manner as long as the jet has sufficient momentum to overcome the downward buoyancy force that hinders the upward motion of the cooler jet.

## 2 Cryogenic Tank Model

This paper considers a large spherical tank in microgravity filled with liquid cryogen and its saturated vapor as illustrated in Fig. 1. This is similar to the model developed previously to study ground-based pressurization [3] except for the initial configuration of liquid and vapor. Here, it is assumed that the vapor region is, at least initially, spherical and completely surrounded by liquid. A cylindrical coordinate system is used with the origin at the center of the tank and with the $z$-axis antiparallel to the direction of gravity. A typical average acceleration for microgravity is assumed to be $g = 981 \times 10^{-6}$ cm/s, and this constant value is used here. Comparisons are also made to solutions obtained in zero gravity. The problem is assumed to be axisymmetric with respect to the $z$-axis.

The liquid is treated as an incompressible, Newtonian fluid with constant density $\rho_\mathrm{l}$, viscosity $\mu_\mathrm{l}$, thermal conductivity $k_\mathrm{l}$ and specific heat $c_\mathrm{l}$. It is described by the standard time-dependent Navier–Stokes, energy and continuity equations. The Boussinesq approximation is used to account for buoyancy effects with thermal expansion coefficient $\beta_\mathrm{l}$.

Fig. 1. The liquid-vapor configuration assumed for the present space-based tank model.

The tank is heated by prescribing the steady heat flux $q_{\mathrm{w}}$ uniformly across the entire tank wall surface. To counter this heating effect, a subcooled liquid jet enters from the bottom of the tank. The jet has a parabolic velocity profile across the inlet area $r < r_{\mathrm{j}}$ with average speed $w_{\mathrm{j}}$ and is maintained at the constant temperature $T_{\mathrm{j}}$. Liquid is removed from the tank through an outlet between $r_{\mathrm{n}} < r < r_{\mathrm{o}}$ at the same mass flow rate in order to preserve mass.

The vapor is treated as an inviscid, compressible, ideal gas with spatially-uniform temperature $T_{\mathrm{v}}$, pressure $p_{\mathrm{v}}$ and density $\rho_{\mathrm{v}}$. It is assumed to be in thermal equilibrium with the surrounding liquid as dictated by the Clausius–Clapeyron equation, so the vapor temperature is equal to the saturation temperature $T_{\mathrm{s}}$ corresponding to the vapor pressure.

The temperature at the liquid-vapor interface is also set equal to the saturation temperature corresponding to the vapor pressure. This interface is treated as a free surface with surface tension $\sigma$ for the first set of short-duration results, but for longer-duration studies, the vapor region is assumed to be spherical and fixed near the wall. Even though the shape of the vapor region is fixed, fluid is still allowed to flow over its surface by imposing a zero tangential-stress boundary condition at the interface.

A lumped-vapor model determines the vapor pressure rise due to any net heat and mass transfer into the vapor region. The original derivation of this model is given in [3] and further details can be found there. The final result is a single evolution equation for the vapor pressure,

$$\frac{\mathrm{d}p_{\mathrm{v}}}{\mathrm{d}t} = F(p_{\mathrm{v}})Q, \tag{1}$$

Table 1
Material properties of hydrogen at the normal boiling point temperature (20.39 K) and other model parameters.

| parameter | value |
|---|---|
| $\beta_{\mathrm{l}}$ | 0.0175 1/K |
| $c_{\mathrm{v}}$ | $1.012 \times 10^8$ erg/K g |
| $c_{\mathrm{l}}$ | $9.7 \times 10^7$ erg/K g |
| $k_{\mathrm{l}}$ | 12440 erg/cm s K |
| $\mu_{\mathrm{l}}$ | $1.327 \times 10^{-4}$ g/cm s |
| $\rho_{\mathrm{v}}$ | 0.00133 g/cm$^3$ |
| $\rho_{\mathrm{l}}$ | 0.07047 g/cm$^3$ |
| $g$ | $981 \times 10^{-6}$ cm/s$^2$ |
| $L$ | $4.456 \times 10^9$ erg/g |
| $m$ | 2.0 g/mol |
| $R_{\mathrm{G}}$ | $8.31 \times 10^7$ erg/K mol |
| $\sigma$ | 1.93 dyn/cm |
| $R$ | 150 cm |
| $r_{\mathrm{j}}$ | 15 cm |
| $r_{\mathrm{n}}$ | 21 cm |
| $r_{\mathrm{o}}$ | 33 cm |
| $q_{\mathrm{w}}$ | 0.01 mW/cm$^2$ |
| $w_{\mathrm{j}}$ | $0.005, 0.05, 0.5$ cm/s |
| $T_{\mathrm{j}}$ | 20 K |

where $Q$ is the net heat entering the vapor region, and $F$ is a complicated function given by

$$F(p_{\mathrm{v}}) = \frac{L}{V_{\mathrm{v}}}\left\{c_{\mathrm{v}}T_{\mathrm{s}} + \left(\frac{Lm}{R_{\mathrm{G}}T_{\mathrm{s}}} - 1\right)\frac{\rho_{\mathrm{l}}}{\rho_{\mathrm{l}} - \rho_{\mathrm{s}}}\left[L - p_{\mathrm{v}}\left(\frac{1}{\rho_{\mathrm{s}}} - \frac{1}{\rho_{\mathrm{l}}}\right)\right]\right\}^{-1}, \tag{2}$$

where $L$ is the latent heat of vaporization, $V_{\mathrm{v}}$ is the vapor volume, $c_{\mathrm{v}}$ is the vapor specific heat at constant volume, $m$ is the molar mass of the cryogen, $R_{\mathrm{G}}$ is the ideal gas constant and $\rho_{\mathrm{s}}$ is the vapor density at the saturation temperature. The property values used here are listed in Table 1.

The net heat flow into the vapor, $Q$, is obtained by integrating the liquid-side heat flux over the entire free surface. As the vapor temperature rises, so does the interfacial saturation temperature. As the interfacial temperature rises, this may change the temperature gradient on the liquid side of the interface, which would change the value of $Q$. This is how the liquid and vapor regions are coupled together.

Comparisons are also made to a lumped thermodynamic model of the entire tank, which assumes that the temperature and pressure are uniform throughout the liquid region as well. The details of this simpler model can also be found in [3].

The governing equations are solved by using an in-house modified version of the commercial finite element code FIDAP [27]. It is modified to include the coupled solution of the lumped-vapor analysis along with the standard solution of the Navier–Stokes, energy and continuity equations for the liquid region. More details about this approach and studies of the spatial and temporal convergence for a similar problem can be found in [3]. At each timestep, an iterative solution strategy is employed with a relative convergence tolerance of $10^{-6}$. Timesteps are chosen adaptively to keep an estimate of the time truncation error less than $10^{-5}$. The number of elements in the mesh varies from between 1470 and 5178, depending on the case, and the mesh is refined in regions of steeper solution gradients. The optimum mesh for each case is determined by successively refining the grid until spatial convergence is achieved. The mesh deforms using the method of spines as the vapor region moves.

## 3 Results and Discussion

To study this problem over the whole range of pertinent timescales, three cases are considered. In the first case, the spherical vapor bubble is assumed to be initially at the center of the tank, and the history of the tank pressure as well as the evolution of the liquid flow and thermal fields are examined by following the deforming bubble as it approaches the tank wall. Its motion is driven solely by the liquid-vapor buoyancy force.

Since the timescale for this process is much shorter than the conduction or convection timescales, the second case study focuses on the temperature, pressure and flow fields that develop over a longer time span while the vapor bubble remains in a fixed position near the tank wall. The free-surface boundary conditions are replaced by a zero shear-stress boundary condition that permits fluid slip over the interface. In this way, the average long-term pressurization of the tank can be studied more efficiently by taking larger timesteps.

Finally, the third case examines the possibility of controlling the tank pressure in microgravity by using a subcooled liquid jet with the vapor region still fixed near the wall. Three different jet speeds are considered, spanning three orders of magnitude. For each jet speed, the time required to bring the pressure back down to its initial value is determined. Comparisons are also made between the microgravity and zero gravity environments.

The results are presented in terms of the history of the vapor pressure, vapor (saturation) temperature, and the net heat flow into the vapor region. Repre-

Fig. 2. Isotherms and streamlines after (a) 259 s, (b) 463 s and (c) 567 s as the initially-centered spherical vapor bubble rises due to buoyancy. The minimum temperature is 20 K and the maximum temperature is (a) 20.00012 K, (b) 20.0058 K and (c) 20.0072 K.

sentative flow and temperature fields in the liquid region are also presented at given times. These fields are depicted by ten temperature and/or streamline contours equally-spaced between the minimum and maximum values. In order to save space and because the solution is axisymmetric, these are combined into a single image with the isotherms on the left and streamlines on the right. The following results are limited to a 95% full (by volume) tank.

Fig. 3. The pressure rise and net heat input into the vapor region for the case shown in Fig. 2.

### *3.1 Case 1: Moving Vapor Region*

The vapor region is initially spherical and located at the center of the tank. The initial temperature is 20 K. As shown in Fig. 2, buoyancy effects are significant enough to bring it near the tank wall in a short period of time. This is not really that surprising when you consider that a similar result could be obtained by a simple calculation based on the tank acceleration $g$ and the initial distance between the vapor and tank wall. For a 95% full tank, the radius of the spherical vapor region is 55.26 cm, and the initial distance between the vapor and tank wall is 150 cm − 55.26 cm = 94.74 cm. The time required for the tank to travel that distance is $(2 \cdot 94.74/g)^{\frac{1}{2}} = 439$ s, and this is close to the time predicted by the model.

The corresponding vapor pressure curve in Fig. 3 shows that there is hardly any change in pressure until the vapor gets very close to the wall. The simulation is eventually terminated when the liquid layer between the interface and the tank wall becomes too thin to be meaningfully resolved.

While the vapor region is being pushed up against the wall, it receives an extra amount of heat as evidenced by the sharp upward spike in $Q$ as indicated in Fig. 3. However, once it begins to retract from the wall as surface tension forces try to restore its spherical shape, it no longer receives as much heat and $Q$ decreases. Near the end of the simulation, the bubble has moved so far away from the wall that it receives hardly any additional heat, and, in fact,

Fig. 4. The initial (a) pressure rise and (b) net heat input when the vapor region is spherical and fixed near the wall.

$Q$ becomes slightly negative as the excess heat stored in the vapor region gets released into the subcooled bulk liquid.

Note that there are a number of high frequency oscillations in $Q$ after the initial peak. These are due to very short timescale events such as the surface oscillations and vortex shedding caused by the draining liquid film between the bubble and tank wall. Interestingly, the corresponding pressure curve does not exhibit these oscillations, because according to Eq. (1), the pressure responds more to the integral of $Q$ over a longer time scale, and shorter duration fluctuations tend to cancel each other out.

### *3.2 Case 2: Tank Pressurization With the Vapor Region Near the Wall*

The previous case study implied that after a relatively short period of time in microgravity, the vapor region will migrate close to the tank wall provided there is no major change in the average direction of the residual acceleration vector during that time. In order to investigate the long-term pressurization without having to take the small timesteps required to resolve the free-surface oscillations, the spherical vapor bubble is now positioned at the wall with only a 1 mm liquid gap between the interface and the wall. The vapor region is not allowed to move from this position or deform from its spherical shape, but liquid is allowed to slip over its surface. The initial pressure rise does depend

Fig. 5. Final isotherms and streamlines after 75 days (right before the jet is turned on) when the spherical vapor bubble is fixed near the wall. Minimum and maximum temperatures are 21.85 K and 22.27 K respectively.

Table 2
Predicted maximum superheat $\Delta T_{\text{sup}}$ (K) and subcooling $\Delta T_{\text{sub}}$ (K) for all of the cases considered here.

| $w_{\text{j}}$ | $\Delta T_{\text{sup}}$ | $\Delta T_{\text{sub}}$ |
|---|---|---|
| microgravity after 75 days: | | |
| 0 | 0.137 | 0.282 |
| microgravity after 150 days: | | |
| 0.005 | 0.148 | 3.80 |
| 0.05 | 0.383 | 0.019 |
| 0.5 | 0.125 | 0.001 |
| zero gravity after 75 days: | | |
| 0 | 0.271 | 0.304 |
| zero gravity after 150 days: | | |
| 0.05 | 0.559 | 0.021 |

on the shape of the vapor region [26], but for the purpose of demonstrating the control strategy, only a spherical vapor region is considered presently.

At first, there is an oscillatory transient response as the fluid flow and temperature fields adjust to this sudden change in heat input. This is exhibited by the fluctuations in the pressure and net heat flow curves of Fig. 4 and is due primarily to a competition between two convection cells in the tank. One arises because of the thermal boundary layer at the tank wall and brings superheated fluid up to the interface. There is an additional thermal boundary layer that arises next to the liquid-vapor interface because the saturation temperature is rising faster than the surrounding subcooled liquid. This drives the other convection cell that brings subcooled fluid up to the interface.

Fig. 6. The long-term (a) vapor pressure, (b) vapor temperature and (c) net heat input both before and after the subcooled jet has been turned on.

Eventually, the temperature and flow fields settle down into a nearly-stationary spatial configuration as shown in Fig. 5, and the heat flux approaches a nearly-constant value as a result. The rate of pressurization then agrees very well with that predicted by the purely thermodynamic model of the entire tank as shown in Fig. 6.

After 75 days, the maximum superheat is 0.137 K and occurs on the tank wall at a point that is 7.4 cm below the top of the tank. The maximum subcooling is 0.282 K and occurs at a point in the liquid that is 16 cm above the bottom of the tank along the symmetry axis. The saturation temperature at this time is 22.13 K. These superheat and subcooling values are listed in Table 2 along with the values for all the other cases considered here.

Note that there is significant thermal stratification in the liquid due to natural convection. There is no such stratification in the corresponding zero-gravity solution [26], showing that buoyancy is still playing a significant role in microgravity even though it acts over a timescale that is much larger than on the ground. The maximum flow speed due to natural convection for the case shown in Fig. 5 is 0.00313 cm/s at a point on the liquid-vapor interface that is about 17 cm above the center of the vapor region. Even though this is very slow, it has an accumulative effect over the long time span considered here.

The extent of thermal stratification can be understood by considering that the intensity of natural convection, as measured by the Grashof number $\mathrm{Gr} = g\beta_\mathrm{l}\rho_\mathrm{l}^2 q_w R^4/k_\mathrm{l}\mu_\mathrm{l}^2$, is a very rapidly increasing function of the tank radius while it is only linearly proportional to the gravitational acceleration. For the large tank in microgravity considered here, $\mathrm{Gr} = 1.97 \times 10^7$. This is very close to the value $\mathrm{Gr} = 2.4 \times 10^7$ for the smaller 10 cm diameter ground-based cryogenic tank considered previously in [3] for which there was also significant thermal stratification. For both cases, the Prandtl number is the same. Thus, it is not surprising that a similar level of thermal stratification is observed here.

### *3.3 Case 3: ZBO Pressure Control With a Subcooled Liquid Jet*

After 75 days of self-pressurization, the subcooled jet is turned on and its effect on the pressure and temperature rise is determined for an additional 75 days as shown in Fig. 6. This is done for three jet speeds spanning three orders of magnitude. Note that the thermodynamic curve does not continue after the first 75 days since there is no easy way to account for the transient cooling effect of the jet in the simple thermodynamic tank model.

It is assumed that the vapor region remains nearly spherical despite the influence of the jet since the ratio of the jet's inertia to surface tension forces, as given by the Weber number $\mathrm{We} = \rho_\mathrm{l} w_\mathrm{j}^2 r_\mathrm{j}^2/2\sigma R$, is only $\mathrm{We} = 0.00685 \ll 1$ for the largest jet speed considered here.

For the lowest jet speed of $w_\mathrm{j} = 0.005$ cm/s, the pressure and temperature continue to rise at nearly the same rate as before since the jet is unable to penetrate far enough into the liquid region to reach the vapor. As shown in Fig. 7(a), the temperature and flow field surrounding the vapor region are nearly the same as before the jet is turned on, and the thermal stratification is hardly disrupted since the cooling effect of the jet is limited to the bottom of the tank. As a result, the net heat flow into the vapor is only slightly decreasing as shown in Fig. 6(c), and this is insufficient to cause any noticeable change in the pressure rise. At its lowest speed, the jet cannot effectively control the

Fig. 7. Final isotherms and streamlines after 150 days for a jet speed of (a) $w_{\mathrm{j}} = 0.005$ cm/s, (b) $w_{\mathrm{j}} = 0.05$ cm/s and (c) $w_{\mathrm{j}} = 0.5$ cm/s. The minimum temperature is 20 K and the maximum temperature is (a) 23.95 K, (b) 20.4 K, (c) 20.13 K.

pressure over the time span considered here.

The final maximum superheat and subcooling for this case are listed in Table 2. Note that the subcooling is so large because the jet is unable to penetrate into the liquid, so it has hardly any cooling effect at all. The subcooling is localized to just near the jet entrance and exit. The superheat is nearly unchanged.

There are two principal reasons why the jet at this speed is unable to penetrate into the tank. First, as shown in the previous section, the maximum speed due to natural convection alone is 0.00313 cm/s, and this is comparable to the jet speed. Second, and perhaps more importantly, is the downward buoyancy force of the subcooled jet itself. As the jet enters the tank, its temperature is 20 K, and this is 2.13 K less than the saturation temperature at that time. Since the jet fluid is so much cooler than the surrounding liquid, there is a strong downward buoyancy force experienced by the jet fluid which resists its upward motion and keeps it near the bottom of the tank.

When the jet speed is increased by an order of magnitude to $w_{\mathrm{j}} = 0.05$ cm/s, it becomes much more effective, but it takes about 2.8 days before the onset of any significant cooling effect since it takes that long for the cooler jet fluid to reach the interface. Obviously, this is much slower than the timescale of about 1.05 hr that is predicted by a simple calculation based on the jet speed and the distance to the vapor.

Since the jet speed is now about 16 times larger than the speed due to natural convection, that is no longer a principal factor, but, instead, this discrepancy in jet penetration time is due mostly to the downward buoyancy force of the cooler jet fluid itself. This downward force is very strong because the jet fluid is about 2 K cooler than the surrounding liquid, and buoyancy acts to keep the cooler fluid at the bottom of the tank. Hence, the jet fluid takes much longer to reach the vapor than it would in the complete absence of buoyancy effects. Again, this shows that buoyancy for such a large tank is still important even in microgravity.

Once cooling begins, it takes another 45 days or so for the jet to bring the saturation temperature and vapor pressure back down to their initial values. This time, the cooler jet fluid penetrates into the liquid region and encapsulates the entire vapor region as indicated by the final isotherms in Fig. 7(b). Even so, there is still some thermal stratification in the remainder of the liquid. The final maximum superheat and subcooling are also listed in Table 2. Note that despite the fact that the subcooling is much smaller now because the cooler jet fluid encapsulates the vapor region, the superheat is even larger than before.

The cooling effect is further enhanced when the jet speed is increased by another order of magnitude to $w_{\mathrm{j}} = 0.5$ cm/s. In this case, the pressure and temperature start dropping after only 6 min, which is in better agreement with the timescale based solely on distance and jet speed. The downward buoyancy force of the subcooled jet is now much weaker when compared to the jet's increased momentum.

Once cooling begins, it only takes about 5 hr for the jet to bring the saturation temperature and vapor pressure back down to their initial values. The final temperature profile also shows that the recirculation of cooler fluid due to the jet flow now encompasses over half of the liquid volume, and the circulation

Fig. 8. Comparison between microgravity and zero gravity pressure control when the jet speed is $w_\mathrm{j} = 0.05$ cm/s. The (a) vapor pressure, (b) vapor temperature and (c) net heat input.

cell due to natural convection is much weaker and only limited to a small region near the bottom of the tank. As a result, thermal stratification in the liquid has been almost entirely disrupted by the jet. This is also reflected in the lower superheat and subcooling values listed in Table 2.

The assertion made earlier (that buoyancy is responsible for slowing the jet penetration) is verified by running another case with jet speed $w_\mathrm{j} = 0.05$ cm/s but without any buoyancy forces (zero gravity) and comparing to the previous microgravity solution. This is done in Fig. 8, and it is clear that there is a significant difference due to buoyancy. In zero gravity, it only takes about

Fig. 9. Comparison of jet penetration times with the same jet speed of $w_{\mathrm{j}} = 0.05$ cm/s for both microgravity and zero gravity environments. Isotherms and streamlines just as the subcooled jet reaches the vapor, which takes (a) 2.8 days in microgravity but only about (b) 1.1 hr in zero gravity. Minimum temperature is 20 K and maximum temperature is (a) 22.34 K and (b) 22.22 K.

1.1 hr for the jet to reach the vapor compared to the 2.8 days predicted for microgravity, and this is in better agreement with the simpler calculation based on jet speed and distance that was predicted to be about 1.05 hr.

The isotherms and streamlines are compared in Fig. 9 at the time when the jet first reaches the vapor region. There is noticeable thermal stratification in the bulk liquid for the microgravity case that is absent in the zero gravity case. As shown in Table 2, the superheat and subcooling are generally higher in zero gravity than in microgravity because of the absence of any mixing effects due to natural convection. Before the jet is turned on, the pressure curve for zero gravity is closer to purely thermodynamic predictions, because in microgravity, natural convection brings warmer fluid up to the interface, leading to a more rapid initial pressure rise. After the initial transient, the slope of both curves agrees with thermodynamics even though the actual pressures are quite different.

## 4 Conclusions

In this paper, we have carefully examined the pressurization of a large liquid hydrogen storage tank in microgravity, and we have demonstrated the feasibility of zero boil-off (ZBO) pressure control using a subcooled liquid jet through a number of parametric numerical case studies.

The results show, somewhat surprisingly, that buoyancy and natural convection are still important in microgravity and cannot be ignored when predicting the pressurization of large cryogenic tanks in space. First and foremost, it is clear that for such large tanks in space, typical average residual accelerations are enough to rapidly move the vapor region up to the tank wall as compared to the conduction and natural convection time scales. Thus, when considering this class of problems, the overall location of the vapor region can be predicted with some degree of certainty if the temporally-averaged direction and magnitude of the acceleration vector are known.

Because of this tendency of the vapor region to move rapidly towards the tank wall, the long-term tank pressurization was studied with the vapor region fixed near the tank wall. However, the reader is cautioned that these predictions should only be regarded as depicting average long-term trends, especially since the short-term microgravity simulations presented here clearly indicate that oscillations of the free surface can lead to short-term fluctuations in the total heat flow into the vapor region. Nevertheless, these fluctuations still occur on a timescale much shorter than the other important transport-related timescales of this problem, so the predicted long-term trends can still be regarded as largely valid.

It was shown that for relatively large tanks such as the one considered here, natural convection plays a significant role, even in microgravity, because there is pronounced thermal stratification in the liquid that is clearly due solely to the effects of natural convection. After a lengthy initial transient response, the rate of tank pressurization eventually agrees with purely thermodynamic predictions even though the final pressure levels are quite different mainly because of these initial transients. The pressurization curve for zero gravity more closely follows thermodynamics as compared to microgravity because of different initial transients.

It is also shown that a subcooled jet can control the tank pressure in microgravity as long as it is strong enough to penetrate through the liquid and encapsulate the vapor region. The jet penetration is hindered by its own intrinsic buoyancy force since the jet fluid is so much cooler than the surrounding liquid as it first enters the tank. The downward buoyancy force opposes the jet's upward motion and increases the amount of time required for the jet to reach the vapor region and initiate cooling. For a fast enough jet, the buoyancy force becomes less important when compared to the jet's momentum, and cooling can be achieved much more rapidly.

## 5 Acknowledgments

This work was supported by NASA OBPR through the Microgravity Division at NASA Glenn Research Center. Additional resources were provided by the Computational Microgravity Laboratory and the Microgravity Fluids Physics Branch at NASA Glenn Research Center.

## References

[1] L. J. Salerno, P. Kittel, Cryogenics and the human exploration of mars, Cryogenics 39 (1999) 381–388.

[2] P. Kittel, D. W. Plachta, Propellant preservation for mars missions, Advances in Cryogenic Engineering 45 (2000) 443.

[3] C. H. Panzarella, M. Kassemi, On the validity of purely thermodynamic descriptions of two-phase cryogenic fluid storage, Journal of Fluid Mechanics 484 (2003) 136–148.

[4] J. C. Aydelott, Effect of gravity on self-pressurization of spherical liquid-hydrogen tankage, NASA TN-D-4286 (1967).

[5] J. C. Aydelott, Axial jet mixing of ethanol in cylindrical containers during weightlessness, NASA TP-1487 (1979).

[6] J. C. Aydelott, Modeling of space vehicle propellant mixing, NASA TP-2107 (1983).

[7] C. S. Lin, M. M. Hasan, N. T. Van Dresar, Experimental investigation of jet-induced mixing of a large liquid hydrogen storage tank, AIAA-94-2079 (1994).

[8] L. J. Poth, J. R. Van Hook, Control of the thermodynamic state of space-stored cryogens by jet mixing, Journal of Spacecraft 9 (1972) 332–336.

[9] C. S. Lin, M. M. Hasan, Self pressurization of a spherical liquid hydrogen storage tank in a microgravity environment, AIAA-92-0363 (1992).

[10] D. A. Vaughan, G. R. Schmidt, Analytical modeling of no-vent fill process, Journal of Spacecraft 28 (1991) 574–579.

[11] Y. S. Cha, R. C. Neiman, J. R. Hull, Thermodynamic analysis of helium boil-off experiments with pressure variations, Cryogenics 33 (1993) 675–679.

[12] G. D. Grayson, D. A. Watts, J. M. Jurns, Thermo-fluid-dynamic modeling of a contained liquid in variable heating and acceleration environments, ASME Publication FEDSM97-3567 (1997).

[13] C. S. Lin, M. M. Hasan, Numerical investigation of the thermal stratification in cryogenic tanks subjected to wall heat flux, AIAA-90-2375 (1990).

[14] J. Navickas, Prediction of a liquid tank thermal stratification by a finite difference computing method, AIAA-88-2917 (1988).

[15] G. D. Grayson, J. Navickas, Interaction between fluid dynamic and thermodynamic phenomena in a cryogenic upper stage, AIAA-93-2753 (1993).

[16] C. S. Lin, M. M. Hasan, Vapor condensation on liquid surface due to laminar jet-induced mixing: The effects of system parameters, AIAA-90-0354 (1990).

[17] J. I. Hochstein, P. M. Gerhart, J. C. Aydelott, Computational modeling of jet induced mixing of cryogenic propellants in low-g, AIAA-84-1344 (1984).

[18] C. H. Liu, A numerical calculation of time dependant dynamical behavior of liquid propellants in a microgravity environment, Microgravity Sci. Technol. VII/2 (1994) 169–172.

[19] R. J. Hung, K. L. Shyu, Constant reverse thrust activated reorientation of liquid hydrogen with geyser initiation, Journal of Spacecraft and Rockets 29 (1992) 279–285.

[20] D. B. Kothe, C. R. Mjolsness, M. D. Torrey, Ripple: A computer program for incompressible flows with free surfaces, Los Alamos National Laboratory, LA-12007-MS (1991).

[21] R. J. Thornton, J. I. Hochstein, Microgravity propellant tank geyser analysis and prediction, AIAA-2001-1132 (2001).

[22] J. G. Marchetta, J. I. Hochstein, Simulation and dimensionless modeling of magnetically induced reorientation, AIAA-2000-0700 (2000).

[23] J. G. Marchetta, J. I. Hochstein, D. R. Sauter, Simulation and prediction of magnetic cryogenic propellant positioning in reduced gravity, AIAA-2001-0930 (2001).

[24] L. D. Peterson, E. F. Crawley, R. J. Hansman, Nonlinear fluid slosh coupled to the dynamics of a spacecraft, AIAA J. 88-2470 (1989) 1230–1240.

[25] R. J. Hung, C. C. Lee, Effect of a baffle on slosh waves excited by gravity-gradient acceleration in microgravity, Journal of Spacecraft and Rockets 31 (1994) 1107–1114.

[26] C. H. Panzarella, M. Kassemi, Pressurization of spherical cryogenic tanks in space, Journal of Spacecraft and Rockets, in print.

[27] M. S. Engelman, R. L. Sani, Finite element simulation of incompressible flows with free/moving surface, in: Numerical Methods in Laminar and Turbulent Flows, Pineridge Press, Swansea, U.K., 1984.

Fig. 1. The liquid-vapor configuration assumed for the present space-based tank model.

Fig. 2. Isotherms and streamlines after (a) 259 s, (b) 463 s and (c) 567 s as the initially-centered spherical vapor bubble rises due to buoyancy. The minimum temperature is 20 K and the maximum temperature is (a) 20.00012 K, (b) 20.0058 K and (c) 20.0072 K.

Fig. 3. The pressure rise and net heat input into the vapor region for the case shown in Fig. 2.

Fig. 4. The initial (a) pressure rise and (b) net heat input when the vapor region is spherical and fixed near the wall.

Fig. 5. Final isotherms and streamlines after 75 days (right before the jet is turned on) when the spherical vapor bubble is fixed near the wall. Minimum and maximum temperatures are 21.85 K and 22.27 K respectively.

Fig. 6. The long-term (a) vapor pressure, (b) vapor temperature and (c) net heat input both before and after the subcooled jet has been turned on.

Fig. 7. Final isotherms and streamlines after 150 days for a jet speed of (a) $w_{\mathrm{j}} = 0.005$ cm/s, (b) $w_{\mathrm{j}} = 0.05$ cm/s and (c) $w_{\mathrm{j}} = 0.5$ cm/s. The minimum temperature is 20 K and the maximum temperature is (a) 23.95 K, (b) 20.4 K, (c) 20.13 K.

Fig. 8. Comparison between microgravity and zero gravity pressure control when the jet speed is $w_{\mathrm{j}} = 0.05$ cm/s. The (a) vapor pressure, (b) vapor temperature and (c) net heat input.

Fig. 9. Comparison of jet penetration times with the same jet speed of $w_{\mathrm{j}} = 0.05$ cm/s for both microgravity and zero gravity environments. Isotherms and streamlines just as the subcooled jet reaches the vapor, which takes (a) 2.8 days in microgravity but only about (b) 1.1 hr in zero gravity. Minimum temperature is 20 K and maximum temperature is (a) 22.34 K and (b) 22.22 K.

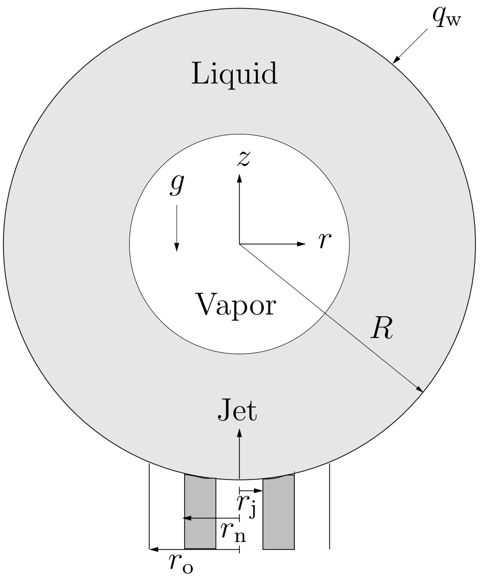
$q_\mathrm{w}$
Liquid
$z$
$g$
$r$
Vapor
$R$
Jet
$r_\mathrm{j}$
$r_\mathrm{n}$
$r_\mathrm{o}$

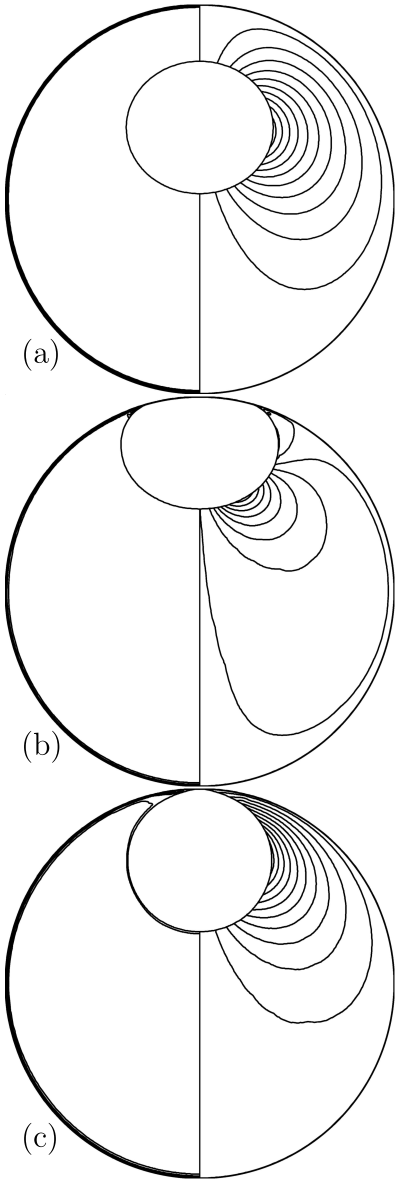
(a)
(b)
(c)

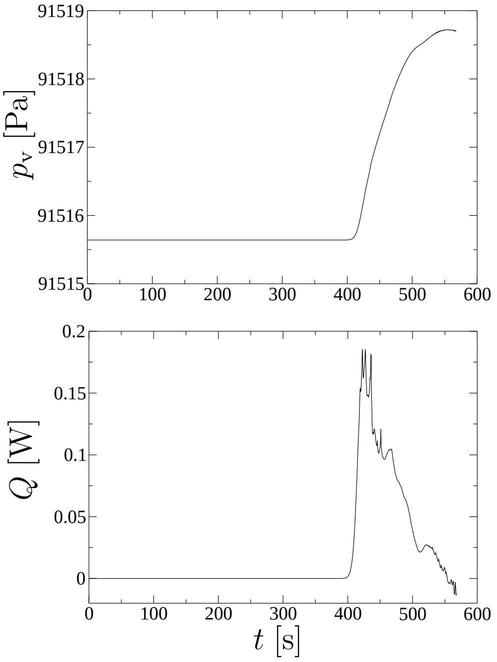
$p_\mathrm{v}$ [Pa]
91519
91518
91517
91516
91515
0
100
200
300
400
500
600
$Q$ [W]
0.2
0.15
0.1
0.05
0
0
100
200
300
400
500
600
$t$ [s]

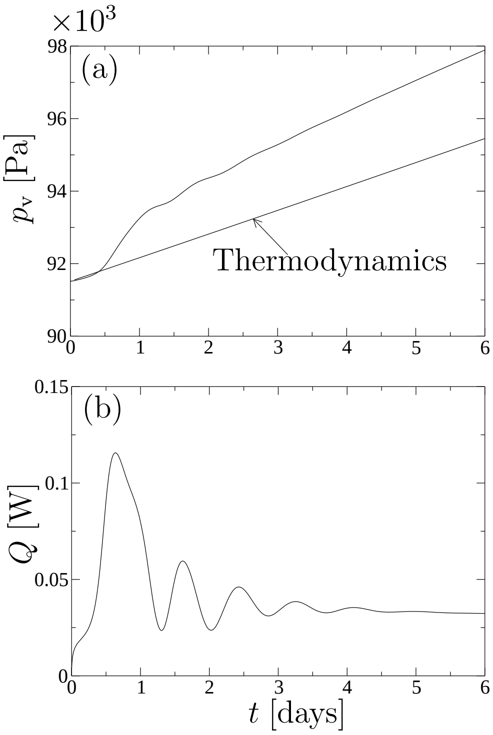
×10^3
(a)
98
96
94
92
90
p_v [Pa]
Thermodynamics
0
1
2
3
4
5
6
(b)
0.15
0.1
0.05
0
Q [W]
0
1
2
3
4
5
6
t [days]

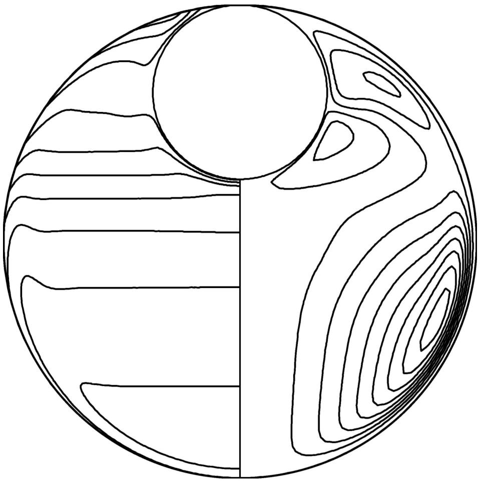

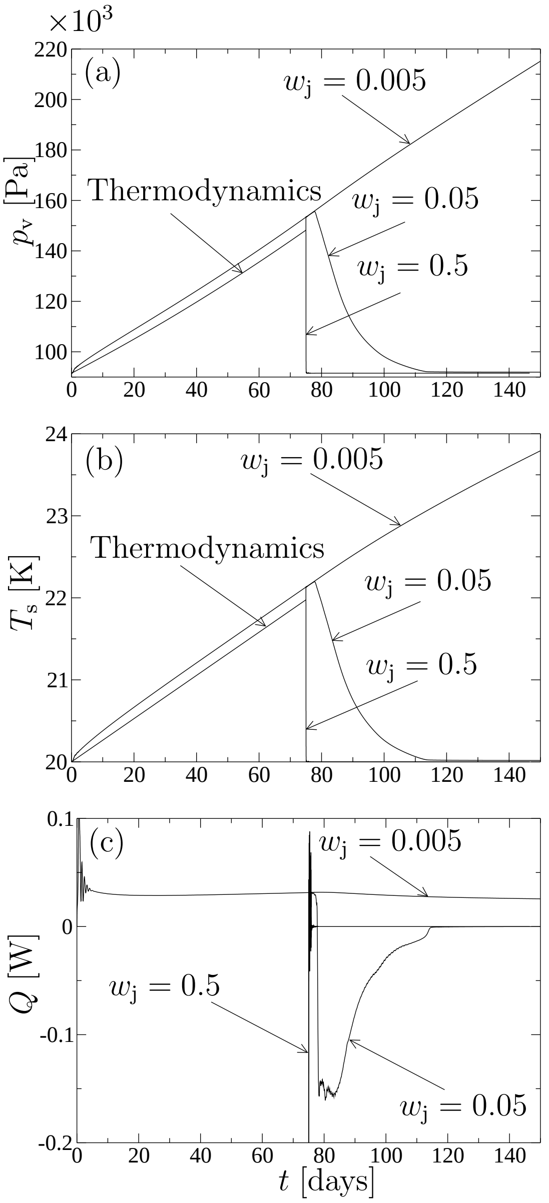
×10^3
(a)
220
200
180
160
140
120
100
$p_\mathrm{v}$ [Pa]
$w_\mathrm{j} = 0.005$
Thermodynamics
$w_\mathrm{j} = 0.05$
$w_\mathrm{j} = 0.5$
0
20
40
60
80
100
120
140
(b)
24
23
22
21
20
$T_\mathrm{s}$ [K]
$w_\mathrm{j} = 0.005$
Thermodynamics
$w_\mathrm{j} = 0.05$
$w_\mathrm{j} = 0.5$
0
20
40
60
80
100
120
140
(c)
0.1
0
-0.1
-0.2
$Q$ [W]
$w_\mathrm{j} = 0.005$
$w_\mathrm{j} = 0.5$
$w_\mathrm{j} = 0.05$
0
20
40
60
80
100
120
140
$t$ [days]

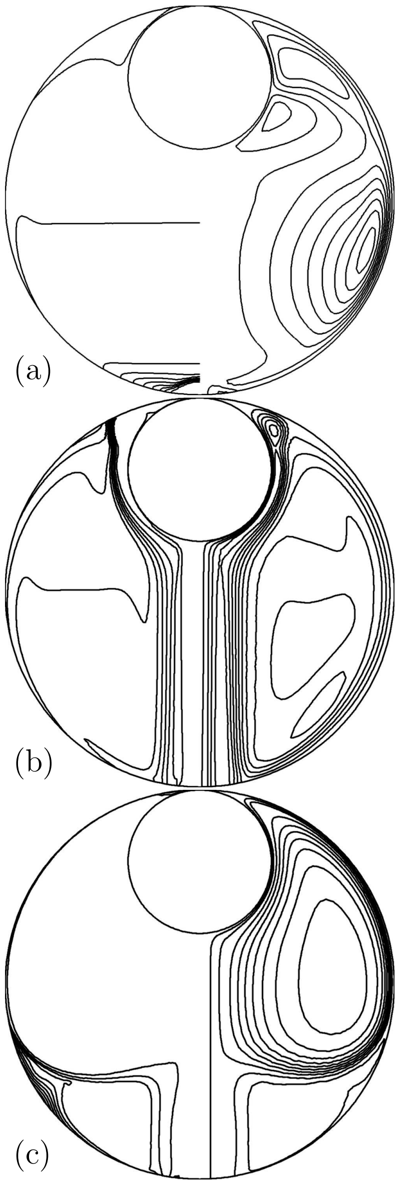
(a)
(b)
(c)

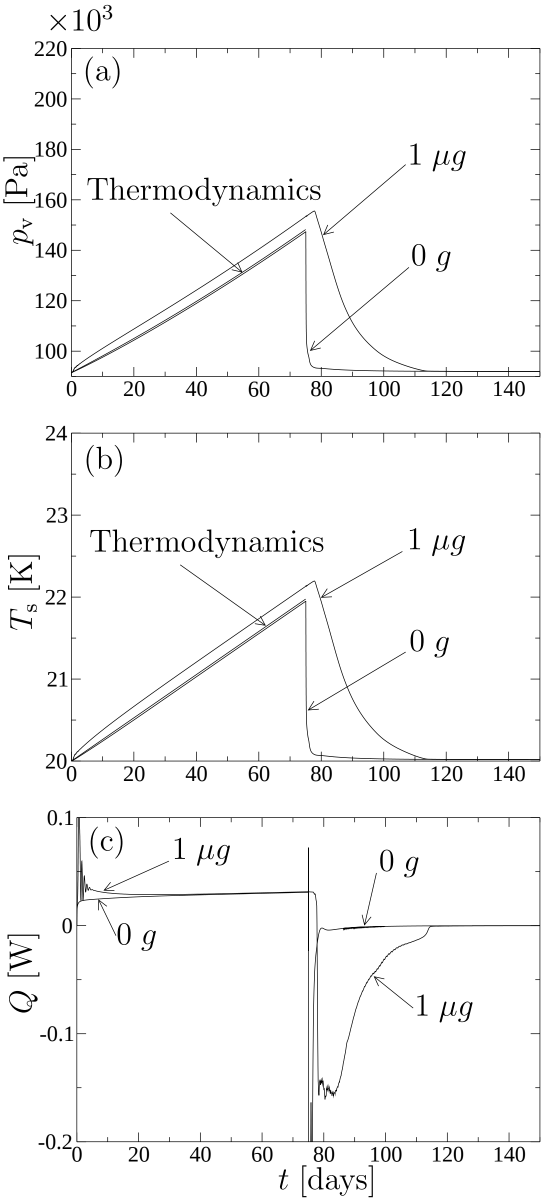
$\times 10^3$
(a)
220
200
180
160
140
120
100
$p_\mathrm{v}$ [Pa]
Thermodynamics
$1\ \mu g$
$0\ g$
0
20
40
60
80
100
120
140
(b)
24
23
22
21
20
$T_\mathrm{s}$ [K]
Thermodynamics
$1\ \mu g$
$0\ g$
0
20
40
60
80
100
120
140
(c)
0.1
0
-0.1
-0.2
$Q$ [W]
$1\ \mu g$
$0\ g$
$0\ g$
$1\ \mu g$
0
20
40
60
80
100
120
140
$t$ [days]

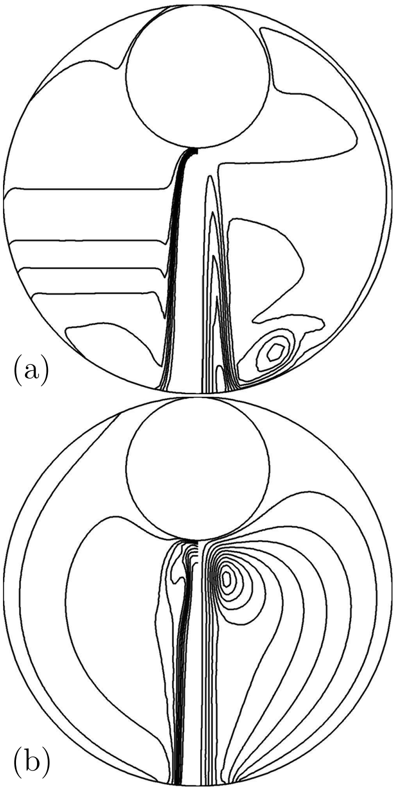
(a)
(b)